ACS APPLIED MATERIALS & INTERFACES

Research Article

www.acsami.org

Plasmonic Effects of Au/Ag Bimetallic Multispiked Nanoparticles for Photovoltaic Applications

Manisha Sharma,[†] Pushpa Raj Pudasaini,[‡] Francisco Ruiz-Zepeda,[‡] Ekaterina Vinogradova,[‡] and Arturo A. Ayon*[,‡]

[†]Department of Chemistry and [‡]Department of Physics and Astronomy, University of Texas at San Antonio, One UTSA Circle, San Antonio, Texas 78249, United States

Supporting Information

ABSTRACT: In recent years, there has been considerable interest in the use of plasmons, that is, free electron oscillations in conductors, to boost the performance of both organic and inorganic thin film solar cells. This has been driven by the possibility of employing thin active layers in solar cells in order to reduce materials costs, and is enabled by significant advances in fabrication technology. The ability of surface plasmons in metallic nanostructures to guide and confine light in the nanometer scale has opened up new design possibilities for solar cell devices. Here, we report the synthesis and characterization of highly monodisperse, reasonably stable, multipode Au/Ag bimetallic nanostructures using an inorganic additive as a ligand for photovoltaic applications. A promising surface enhanced Raman scattering (SERS) effect has been observed for the synthesized bimetallic Au/Ag multispiked nanoparticles, which compare favorably well with their Au and Ag spherical nanoparticle counterparts. The synthesized plasmonic nanostructures were incorporated on the rear surface of an ultrathin planar c-silicon/organic polymer hybrid solar cell, and the overall effect on photovoltaic performance was investigated. A promising enhancement in solar cell performance parameters, including both the open circuit voltage (V_{OC}) and short circuit current density (J_{SC}), has been observed by employing the aforementioned bimetallic multispiked nanoparticles on the rear surface of solar cell devices. A power conversion efficiency (PCE) value as high as 7.70% has been measured in a hybrid device with Au/Ag multispiked nanoparticles on the rear surface of an ultrathin, crystalline silicon (c-Si) membrane (~12 μm). This value compares well to the measured PCE value of 6.72% for a similar device without nanoparticles. The experimental observations support the hope for a sizable PCE increase, due to plasmon effects, in thin-film, c-Si solar cells in the near future.

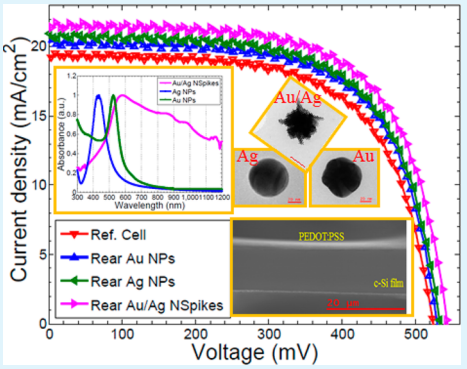

KEYWORDS: *solar cell, light trapping, heterojunction, ultrathin, plasmonics, nanoparticles*

1. INTRODUCTION

Recently, plasmonic effects have gained momentum in solar cell research because they are deemed to be able to dramatically boost the efficiency of both organic and inorganic thin film solar cells.[1−7] A key characteristic of plasmon resonance lies in its ability to condense the conduction electron oscillation strength into the desired spectral range for photovoltaic applications. To this end, silver (Ag) nanoparticle (NP) enabled plasmonic effect has been proposed and demonstrated as a promising approach to achieve light trapping in thin film solar cells because the relative scattering efficiency of Ag NPs is higher than that of other noble metal NPs in the visible range.[8−11] However, due to the resonant nature of the plasmonic effect of the NPs, the useful absorption enhancement can only be realized at certain wavelengths determined by the NP size, shape, composition, and their local dielectric environment.[12−14] Nonetheless, these enhancements are generally offset by a detrimental parasitic absorption at other wavelengths that minimizes the increase in solar cell efficiency. Therefore, broadband optical absorption enhancement is the primary challenge to solve before the plasmonic solar cells can migrate from a laboratory environment. Previous efforts on plasmonic solar cells mainly focused on theoretical modeling and the experimental demonstration of randomly or regularly distributed monometallic NPs or grating structures with rigorous geometry precision requirement.[1−3,15−18] Although, promising efficiency enhancements due to the plasmonic effects of metallic NPs have been reported theoretically, to date the conspicuous experimental efficiency improvement has not been achieved. There are numerous factors which affect the optical absorption enhancement in a thin film solar cell due to the plasmonic effect of metallic NPs. Thus, nanoparticle shape, size, composition, and surrounding dielectric material, to name a few, have to be optimized to couple the incident light to the thin active layer of solar cells. There are at least three ways to employ plasmonic nanostructures for broadband optical absorption enhancement. First, metallic nanostructures can be used as subwavelength scattering elements to couple and trap

Received: June 24, 2014
Accepted: August 19, 2014
Published: August 19, 2014

freely propagating plane waves from the sun in the active layer of the device. Second, metallic nanostructures can be used as subwavelength antennas in which the plasmonic near field is coupled to the semiconductor, thereby increasing its effective absorption cross section. Third, a corrugated metallic film on the back surface of a thin photovoltaic absorber layer can couple sunlight into surface plasmon polariton modes supported at the metal/semiconductor interface. Different groups have studied the effects of plasmonic metal NPs on optical absorption enhancement by incorporating them on the front surface of solar cells, and it has been observed that such an arrangement leads to constructive interference between the transmitted and scattered light, thereby increasing the absorption at wavelengths above the plasmon resonance.[19−23] However, it also leads to destructive interference and, hence, a reduced absorption at wavelengths shorter than that of the plasmon resonance. Therefore, metallic NPs may be considered to be placed on the rear surface of a solar cell to avoid the suppression of the photocurrent at wavelengths below the plasmon resonance. Most previous experimental reports dealing with plasmonic solar cells have focused on spherically shaped silver or gold NPs.[10,24−26] In this paper, we report the synthesis and characterization of highly monodisperse, reasonably stable, Au/Ag bimetallic multispiked NPs using an inorganic additive as a ligand for photovoltaic applications. An efficient approach to produce self-assembled and well-dispersed plasmonic NPs in a porous anodic aluminum oxide (AAO) template is also reported. A promising SERS effect has been observed for the synthesized bimetallic Au/Ag multispiked NPs, which compare favorably well, with their spherical Au and Ag NP counterparts. To achieve noticeable light trapping in an ultrathin c-Si solar cell using plasmonic NPs, a large scattering cross section is highly desirable for the wavelength at which the transmission losses become significant. Moreover, the parasitic absorption in the particle should be minimized, and a large fraction of scattered light should reach the active layer of the solar cell device. The scattering and absorption cross sections, and the coupling efficiency are sensitive to the nanoparticle geometry, the local dielectric environment, and the distance from the semiconductor interface. To maximize the scattering performance of the plasmonic NPs, relatively large size NPs were synthesized (∼90 nm) and were embedded in a 60 nm alumina passivation layer with a 10 nm dielectric spacing between the NPs and the rear surface of the c-Si interface. The planar, c-Si/organic polymer hybrid solar cell devices with different plasmonic NPs on the rear surface were fabricated and the effect of various NPs on photovoltaic performance was investigated.

2. EXPERIMENTAL SECTION

2.1. Synthesis of Plasmonic Metallic Nanostructures. *2.1.1. Synthesis of Au/Ag Bimetallic Multispiked Nanoparticles.* Highly monodisperse, reasonably stable, Au/Ag bimetallic multispiked NPs were synthesized by using a coreduction reaction method for photovoltaic applications. To this end, 10 mL of a 2 mM solution of $AgNO_3$ containing 0.2 g of PVP was stirred for 15 min at room temperature. Then 2 mL of 28% $NH_3{\cdot}H_2O$ was added to the solution, and after stirring for 2 min 5 mL of a 2 mM $HAuCl_4$ solution was added. After an additional 2 min, 0.1 g of KI was added and the mixture was stirred for approximately 15 min. Subsequently, 0.1 mL of 0.1 M ascorbic acid was added. In the overall reaction, PVP is employed as a stabilizer, $NH_3{\cdot}H_2O$ is added to avoid forming a precipitate of AgCl, and ascorbic acid functions as a reducing agent.

2.1.2. Synthesis of Ag Nanospheres. Silver nanoparticles of average size 90 nm were also synthesized by a seed-mediated growth method described elsewhere.[27] To this end, 111 mg of PVP were added to 10 mL of diethylene glycol (DEG) while stirring at 80 °C. PVP acts as a capping agent. After the solution turned clear, 0.25 mL of 0.5 M $AgNO_3$ aqueous solution was injected rapidly. The solution was maintained at 80 °C while continuously being stirred until it turned yellow, then the reaction solution was transferred to a 20 mL autoclave and maintained at 230 °C for 24 h. Subsequently, the solution was allowed to cool down to room temperature. The purification of the NPs was carried out by (i) filtration via a 200 nm pored syringe filter followed by (ii) centrifugation at 2000 rpm for 15 min. Only the upper part of the solution was collected to obtain homogeneous Ag NPs of average size of 90 nm. Finally, the recovered solution was washed several times with deionized water to remove the excess DEG.

2.1.3. Synthesis of Au Nanospheres. Spherical Au NPs of uniform sized were synthesized employing methods described elsewhere.[28] Typically, 1 mL of $HAuCl_4$ (5 mM) and 1 mL of trisodium citrate (TSC) (5 mM) were mixed with 18 mL of H_2O in a flask. Under vigorous stirring, 0.6 mL of freshly made $NaBH_4$ solution (0.1 M) was quickly injected into the solution. After stirring for 4 h, the solution was collected as the seed solution for subsequent seeded growth. Under vigorous stirring, 20 μL of the seed solution was then quickly injected into a freshly prepared growth solution of Au containing 2 mL of PVP (5 wt %), 1 mL of ascorbic acid (0.1 M), 0.8 mL of KI (0.2 M), 240 μL of $HAuCl_4$ (0.25M), and 8 mL of H_2O. After 10 min, the Au NPs formed were collected by centrifugation and redispersed in water. The synthesized Au NPs were all similar with an average particle size of 90 nm as measured with an SEM tool. For further characterization and before employing them in a device, the solution was washed several times in ethanol.

2.2. Preparation of Anodized Aluminum Oxide (AAO) Template. Highly ordered AAO nanochannel arrays are fabricated by a modified two-step anodization process that has been described elsewhere.[29,30] In this scheme, commercially available high purity thin aluminum foils (0.1 mm thick, 99.99% purity, Alfa Aesar) are cleaned with acetone, isopropyl alcohol, and deionized (DI) water each for 1 min in an ultrasonic bath. For the first anodization step, the pore spacing and pore diameters of the porous AAO can be controlled by the electrolyte selected, the anodic voltage, and the temperature maintained during the reaction. The first anodization step was carried out in a 0.3 M oxalic acid solution at 0.5 °C while applying a 60 V anodization voltage for 12 h. Self-ordering of the pores takes place with increasing alumina thickness. This sacrificial alumina layer is then selectively removed in a solution comprising phosphoric acid (6 wt %) and chromium oxide (1 wt %) for 12 h in a furnace at 60 °C, leading to a nanotemplated aluminum substrate. The patterned aluminum substrate is then anodized for a second time under the same experimental conditions used during the first anodization step, leading to a thin alumina layer exhibiting a hexagonal lattice with a thickness dependent on the anodizaton time. As the thickness of the AAO membranes increases, their flexibility decreases. The resulting AAO membrane is released from the aluminum foil using a solution comprising copper sulfate (3 wt %) and hydrochloric acid (30 wt %) for 30 min. The back "barrier layer" of this thin AAO film is removed using chemical wet etching in a pore widening process that was carried out in a phosphoric acid solution (5 wt %) for 1 h at 20 °C, leading to free-standing AAO membranes. An optical image of a free-standing nanochannel AAO membrane floating on water can be seen in Supporting Information Video S1.

2.3. Solar Cell Fabrication. At first, sub-20 μm free-standing silicon membranes were obtained by immersing n-type, double side polished, 4″ silicon (100) wafers with a resistivity of 1−5 Ω-cm in a KOH solution with a concentration of 50 wt % at 90 °C for a sufficient amount of time. Under these conditions, the silicon etching rate was observed to be ∼80 μm/h. The produced free-standing silicon membrane is mechanically flexible, and sturdy enough to tolerate handling with Teflon-coated tweezers and the rigors of clean room processing, including spin-casting, dielectric film deposition, and metallization. Prior to solar cell fabrication, the produced free-standing

ultrathin silicon samples went through a rigorous cleaning procedure. Initially, the samples were cleaned by immersing them in a piranha solution comprising H_2O_2 and H_2SO_4 in a volume ratio of 1:3 at 80 °C for 10 min. Subsequently, the samples were rinsed with DI water and dried with a N_2 gun. The samples were then subjected to a standard RCA cleaning procedure. To this end, the samples were cleaned by immersing them in a solution consisting of H_2O_2 (30%), NH_4OH (37%), and DI water in a volume ratio of 1:1:5 at 80 °C for 30 min. The samples were then transferred to a DI water bath for 10 min. In the next step, the samples were immersed in a solution comprising H_2O_2 (30%), HCl (37%), and DI water in the volume ratio of 1:1:5 at 80 °C for 30 min. Once more, the samples were then transferred to a DI water bath for 10 min. Finally, the samples were cleaned using a diluted HF (2%) solution for 60 s to remove the native oxide. After the described cleaning procedure and regarding the back side processing of the device, the free-standing ultrathin c-Si membrane was taped on a dummy wafer using Kapton tape. Nickel (10 nm)/silver (100 nm) fingers electrodes connected to the bus line as back contacts were defined employing an evaporator and a shadow mask. After this step, an ALD aluminum oxide (Al_2O_3) film, 10 nm thick was deposited on the back side of the devices while protecting the bus lines using Kapton tape. Then 40 μL of each NP aqueous solution (Au, Ag, and Au/Ag) was self-assembled on the back surface of the c-Si thin membrane sample by dispensing the previously prepared NP samples employing a through-hole anodized alumina template. Afterward, another Al_2O_3 film 50 nm thick was deposited on the backside to encapsulate the NPs. Finally, a silver film 300 nm thick was evaporated on the back side of the cell to serve as the back reflector. For the front side processing of the cell, the free-standing ultrathin silicon membrane was taped once more on a dummy wafer using Kapton tape. Then, highly conductive poly(3,4-ethylene-dioxythiophene)/polystyrenesulfonate (PEDOT:PSS) mixed with dimethyl sulfoxide and Triton X-100 solution (surfactant) was spin-cast at 300 rpm for 10 s and 2000 rpm for 60 s to form a hetero p−n junction structure. The samples were then annealed on a hot plate at 140 °C for 30 min to remove the solvents. Finally, a silver film 200 nm thick was evaporated to form a finger grid connected to the bus bar as a front contact. Figure 1a−c depicts the schematic illustration of the fabrication of the described hybrid silicon solar cells with and without different plasmonics nanostructures on the rear surface of the respective device, while Figure 1d shows the cross-sectional view of the fabricated ultrathin c-Si/PEDOT:PSS heterojunction solar cell. We have fabricated and characterized three different devices having (a) Au nanospheres, (b) Ag nanospheres, and (c) Au/Au bimetallic multispiked NPs, on the rear surface of the hybrid cell, as well as the corresponding planar reference device without plasmonic metal NPs for comparison purposes.

2.5. Characterization. The morphology of the NPs was analyzed by using high-resolution scanning electron microscopy (SEM, Hitachi S-5500) with a field emission gun and transmission electron microscopy (TEM, JEOL 2010F) operated at 200 kV. Energy dispersive X-ray spectra (EDS) were obtained using an EDAX instrument installed in a JEOL ARM 200F microscope operated at 200 kV. The optical absorbance spectra of the different metallic NPs were collected by using a UV−vis-NIR (Varian Cary 5000) spectrometer. Raman spectra were collected with an iHR 320 Horiba Jobin Yvon spectrometer using laser excitation with a wavelength of 785 nm and output power of 25 mW. This instrument was equipped with an Olympus BX41 optical microscope and a thermoelectrically cooled charge coupled detector (Synapse CCD Detection System) with 1024 × 256 pixel format, operating at −70 °C. The signal was calibrated by using the 520 cm^{-1} line of a silicon wafer and a 10× objective. The laser beam spot size was about 3.8 μm on the sample. The photovoltaic performance was collected using a solar simulator (Newport Sol2A) under AM 1.5G illumination (1000 W/m^2) at standard testing conditions.

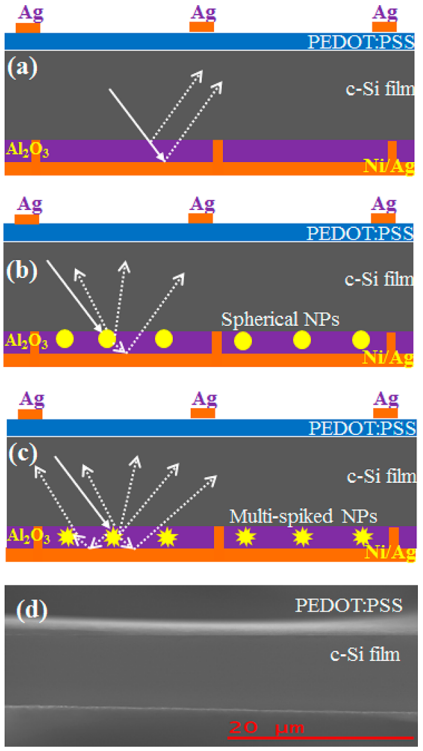

Figure 1. Schematics of the described solar cells based on ultrathin c-Si film and PEDOT:PSS. (a) Without nanoparticles on the rear surface. (b) With spherical gold or silver nanoparticles, showing the random scattering of incident radiation. (c) With multispiked nanoparticles on the rear, indicating the enhanced scattering. (d) Cross-sectional SEM micrograph of the fabricated ultrathin c-Si/PEDOT:PSS hybrid solar cell.

3. RESULTS AND DISCUSSION

3.1. Characterization of Bimetallic Au/Ag Multispiked Nanoparticles. The average size of the Au/Ag multispiked NPs was approximately 90 nm, the largest NP observed was 130 nm, and the smallest measured was 70 nm. Figure 2a shows a TEM image of the Au/Ag multispiked NPs and Figure 2b shows a single particle with spikes of different morphology. The microstructure of the Au/Ag NPs was observed to vary according to the morphology of the nanospikes. Some of the spikes are observed to have more defects than others (see Figure 2c, d and Figure S1 in the Supporting Information). The growth of the spikes was observed to be along the $\langle 01\bar{1} \rangle$ direction of the FCC structure (Figure 2c), and the growth mechanism along this direction involved the creation of defects at the center of the spikes. The formation of twin planes along the longest axis of the spikes $[01\bar{1}]$ suggests that they grow plane symmetrically.[31] Other spikes show the formation of multiple stacking faults, as can be seen in Figure 2d; however, when the growth is along the $\langle 111 \rangle$ direction, the spikes exhibited no defects, showing a single crystal structure.

It has been found that silver nitrate plays a special role on the behavior of gold atoms during growth. Silver assisted growth is slower, and gold atoms would grow a structure with no defect.[32] In other cases, gold atoms would change the stack packing because of the incorporation of silver and the small lattice mismatch between the two species.[33]

To study the chemical composition of the multispiked NPs, EDS analysis was performed at the core of the particle and on one of the spikes (see Figure 3). The gold and silver content

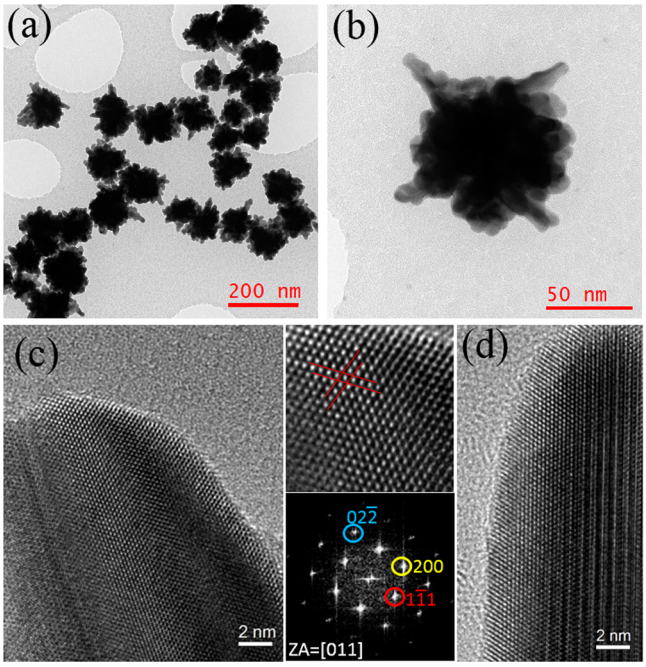

Figure 2. (a) TEM image of the Au/Ag multispiked NPs. (b) Single Au/Ag multispiked NP showing different spike morphologies. (c) HRTEM image of the tip of a spike. Enlarged atomic structure image with FFT pattern showing the [011] orientation and the growth direction along [01$\bar{1}$]. (d) Detailed structure of a different spike, showing multiple defects along the long axis of the spike.

was observed to be distributed along the whole particle as in an alloy (Figure 3a, b). Along the spikes, more silver content was detected at the surface of the spike (Figure 3b–e). The strongest values for the EDS signal were observed at the center of the nanoparticles where the thickness is largest (Figure 3a).

The high contrast observed in the high angle annular dark field (HAADF) image at the core in Figure 3a originates from thickness variations rather than to a difference in atomic number. The contrast in the HAADF image on the spike (Figure 3b) may indicate a variation in the composition distribution since there is no significant thickness variation. The EDS elemental mapping analysis of the spikes showed a homogeneous distribution of rich gold content on the spike. On the other hand, the silver content showed a preferential distribution at the surface of the spike, as it is shown in Figure 3b–e. This behavior was also observed for other spikes (see Supporting Information Figure S2).

The gold and silver spherical NPs of average size of 90 nm were also synthesized by the previously described chemical methods. Figure 4 depicts the SEM micrographs of (a) gold and (b) silver NPs, while the image in the inset of the corresponding figures is the TEM image of a single Au and Ag NP, respectively.

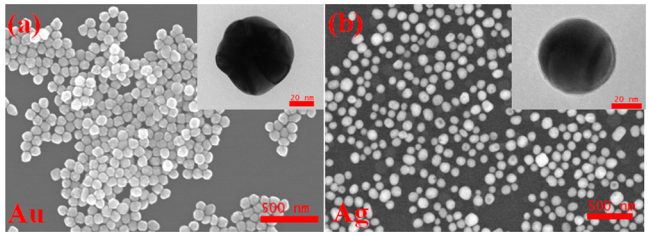

Figure 4. SEM micrographs of (a) Au NPs and (b) Ag NPs. The TEM image of a single Au and Ag NP is included in the corresponding inset.

3.2. Raman scattering and Uv–Vis Measurements. To investigate the Raman enhancement induced by metallic NPs, we measured the Raman scattering of rhodamine 6G (R6G) in an AAO template with and without metallic NPs. The self-

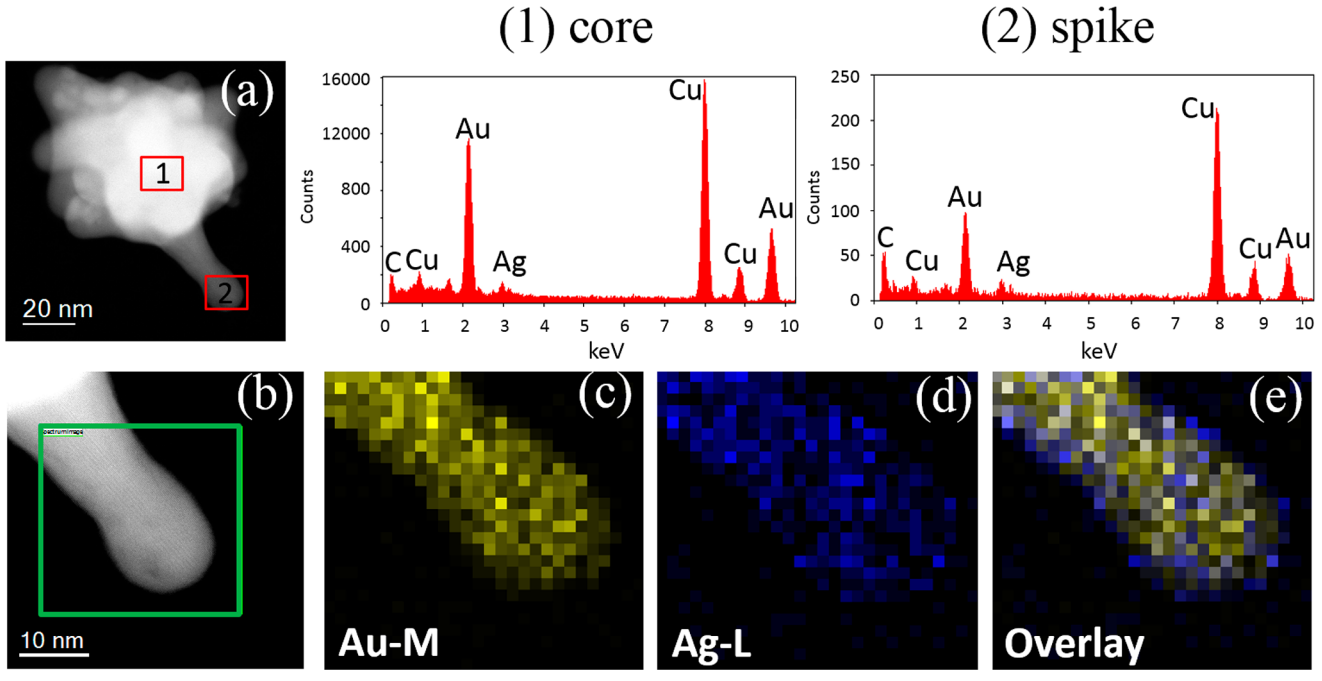

Figure 3. (a) STEM micrograph of a multispiked NPs. EDS data performed at the core (1) and on the spike (2) of the nanoparticle. (b) STEM HAADF and EDS elemental mapping images of the spike. (c) Au-M map, (d) Ag-L map, and (e) an overlay of the Au and Ag maps. Silver content is observed preferentially on the surface of the spike.

dx.doi.org/10.1021/am5040939 | ACS Appl. Mater. Interfaces 2014, 6, 15472–15479

assembled and well-dispersed metallic NPs in the pores of anodized alumina templates were produced by dispensing 40 μL of the previously synthesized NPs solutions on a 1 cm × 1 cm area of the template. Figure 5a–c shows the schematic of the SERS substrate with (see Figure 5c) and without (see Figure 5b) NPs.

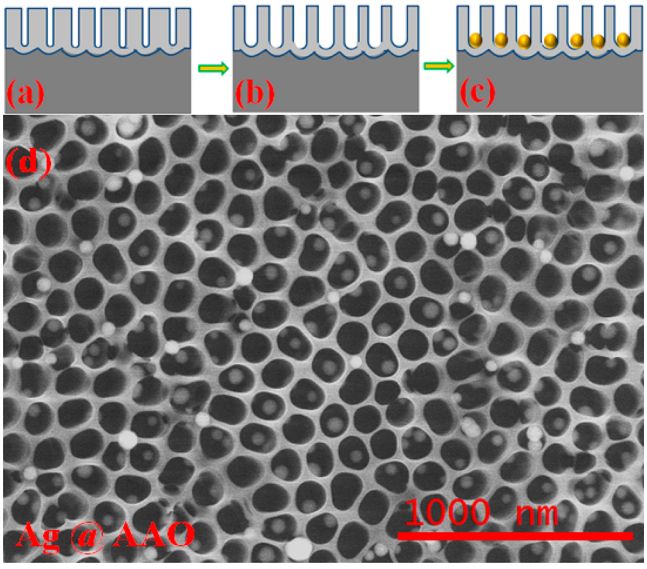

Figure 5. (a–c) Schematics of porous anodized alumina templates used in Raman spectra measurement, (a) before the pore widening, (b) after pore widening, and (c) after decoration with metallic NPs. (d) SEM micrograph of Ag NP decorated AAO template.

Highly ordered hexagonal arrays of nanoporous alumina templates were fabricated by the previously described two-step anodization method. The diameters of the pores were controlled by varying the time in the pore widening process (see Figure 5b). An average pore diameter of 100 ± 10 nm was obtained by widening the pores for 45 min in 6 wt % phosphoric acid at 20 °C. Figure 5d depicts the SEM micrograph of the Ag NPs decorated anodized porous alumina template. More than 90% of the pores were filled with NPs. Finally, to obtain the Raman signal, 20 μL of 0.05 mM R6G dye molecules was dispensed on top of 1 cm × 1 cm area of alumina template with and without metallic NPs. The red curve in Figure 6 represents the Raman scattering intensity of the reference dye molecule on AAO template. Upon integration of the metallic NPs into the AAO pores, there was a substantial increase in the intensity of the R6G Raman bands at 611 (C–C–C ring in-plane bending), 770 (CH out-of-plane bending), 1183 (C–O–C stretching), 1312 (C–C/C–N stretching), 1362 (C–C/C–N stretching), and 1510 and 1650 cm^{-1} (C–C stretching),[34,35] when contrasted with R6G molecule alone on AAO template. It is generally agreed that the dominant contributor to SERS effect is the long-range electromagnetic (EM) enhancement mechanism, which originates from the amplification of the light by excitation of either extended surface plasmon resonances on continuous metal surfaces or localized surface plasmon resonances on isolated noble metal particles.[36] The second mechanism contributing to signal enhancement is the short-range chemical enhancement, which involves changes in the adsorbate electronic states owing to chemisorption of the analyte.[37] The binding between the metal and analyte involves charge transfer which is responsible for the

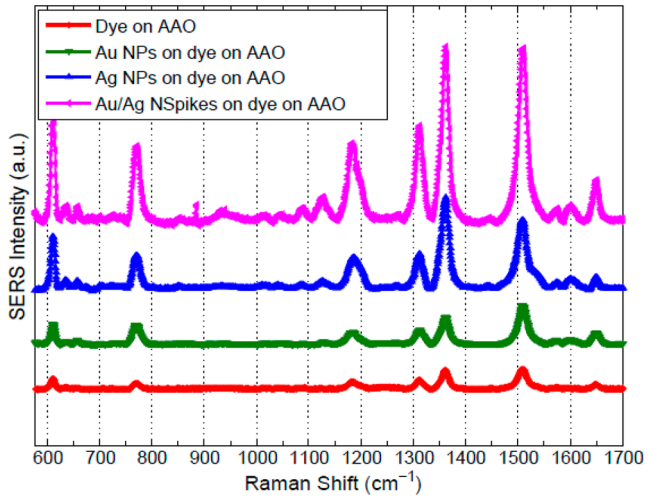

Figure 6. Measured Raman scattering of R6G dye molecules in anodized alumina template with (magenta) and without (red) Au/Ag multispikes nanoparticles. The Raman intensity spectra enhancement due to Au (green curve) and Ag (blue curve) are also plotted for comparison.

shift of some SERS bands to higher or lower frequencies depending on the bond order. Since no valuable differences in band positions of the Raman and SERS spectra of R6G have been observed, it is reasonable to conclude that the SERS enhancement is long-range EM in origin. The enhancement due to the Ag NPs (blue curve in Figure 6) was stronger than the enhancement due to the Au NPs (green curve in Figure 6). Moreover, the presence of Au/Ag multispiked NPs (magenta curve in Figure 6) was even more efficient to enhance the Raman scattering signal. Since the Raman scattering signal is proportional to the electric field intensity, therefore the stronger Raman scattering due to the NPs corresponds to the stronger electric field associated with it. The stronger SERS behavior of Au/Ag bimetallic multispiked NPs, compared to spherical Au and Ag NPs, is due to the anisotropic distribution of the EM field close to the tips of the branched particles, according to the findings reported elsewhere.[38,39] Silver is well-known for its superior optical properties and ability to increase the SERS activity of Au NPs.[40]

Based on the evidence of the presence of silver on the surface of the multispiked particles observed in the EDS element distribution maps, we suggest that the incorporation of silver into the tips increases the EM field enhancement of the associated plasmons, resulting in higher SERS performance. The enhanced magnitude of R6G peaks demonstrated the potential for application of these bimetallic multispiked NPs in an ultrasensitive SERS substrate.[41] To find the plasmonic resonance of the bimetallic Au/Ag multispiked NPs, we measured the UV–vis absorbance spectra.

Figure 7 depicts the normalized absorbance spectra of the synthesized Au/Ag multispiked NPs (magenta curve). The absorbance spectra for Au (green curve) and Ag (blue curve) NPs are also plotted for comparison. More interestingly, a broad plasmonic resonance has been observed for the Au/Ag multispiked NPs in the longer wavelength regions. We believe the spikes with different size, shape, and/or orientations were responsible for the measured broad plasmonic resonance, which is especially important for thin film single crystal silicon solar cells. Most of the short wavelength photons in the solar spectrum are absorbed by a few hundred nanometers of silicon

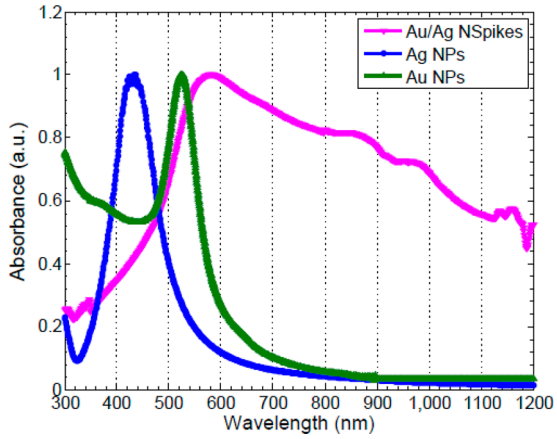

Figure 7. Measured UV−vis spectra for Au/Ag multispiked NPs (magenta curve) as a function of wavelength. The measured spectra of Au (green curve) and Ag (blue curve) NPs are also plotted for comparison.

layer in the front surface of a thin film c-Si solar cell. Therefore, to achieve broad band optical absorption in a thin silicon membrane the long wavelength photons should be effectively trapped within the device. This could be achieved by incorporating these Au/Ag multispikes NPs on the rear surface of the cells.

3.3. Effects of Plasmonic Metal Nanostructure on the Photovoltaic Performance of the Device. An inorganic/organic hybrid solar cell has been considered as a viable alternative for low-cost photovoltaic devices because the Schottky junction between inorganic and organic materials can be formed employing low temperature processing methods.[42−44] The different c-Si/PEDOT:PSS hybrid heterojunction solar cell devices were fabricated on an ultrathin silicon membrane by the previously described fabrication methods. To study the plasmonic effect of the Au/Ag bimetallic multispiked NPs on the PV performance of the solar cells, the previously synthesized NPs were self-assembled on the rear side of devices employing through-hole anodized alumina templates.

Similar devices were also fabricated employing spherical Au and Ag NPs and also a reference cell without plasmonic NPs. The surface coverage due to the metallic NPs was well controlled by dispensing the NPs solution through an anodized alumina template as can be observed in the SEM micrographs included in Figure 8; Figure 8a is a top view of a portion of an alumina template decorated with Ag nanoparticles, while Figure 8b is a cross-sectional SEM micrograph of a through-hole ultrathin alumina template with thickness 400 nm. To verify the barrier layer opening on the template, a film of 40 nm of gold was evaporated on top of the template to observe the Au islands on the underlying silicon substrate. The uniformly distributed self-assembled Ag NPs shown in Figure 8c had a surface coverage of approximately 15%.

Figure 9 depicts the cross section SEM micrograph of the rear side of the cell showing the Au/Ag multispiked particles embedded in an ALD deposited aluminum oxide passivation layer. Similar approach has been applied to embed the Au and Ag NPs on the rear surface with an Al_2O_3 passivation layer (see Figure S3 in the Supporting Information). The fabricated devices were characterized by collecting the current density versus voltage. Figure 10 depicts the measured $J-V$ characteristic curves for the devices with and without Au/Ag bimetallic multispiked NPs on the rear surface of the fabricated solar cells.

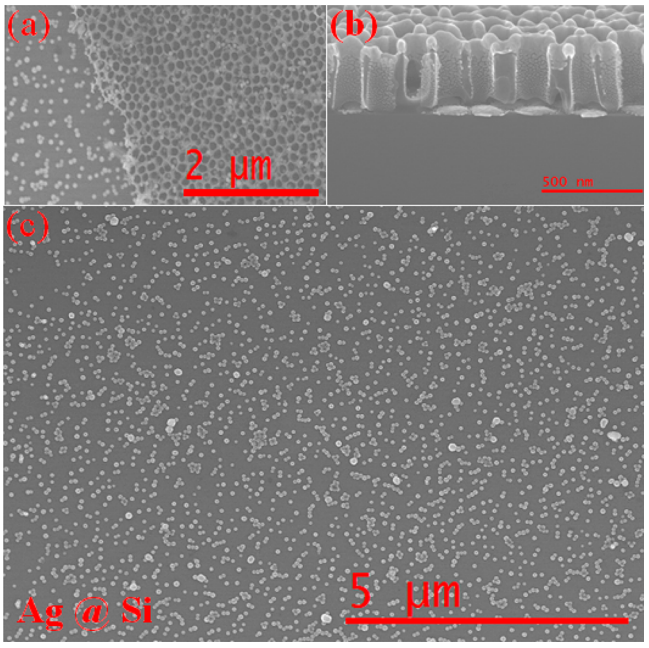

Figure 8. (a) Top view SEM micrograph of self-assembled Ag NPs on an anodized alumina template. (b) Cross-sectional SEM micrograph of an ultrathin anodized alumina template on a silicon substrate. 40 nm Au was evaporated on top of it as a verification of the barrier layer opening. (c) SEM micrograph of self-assembled Ag NPs on silicon using an alumina template.

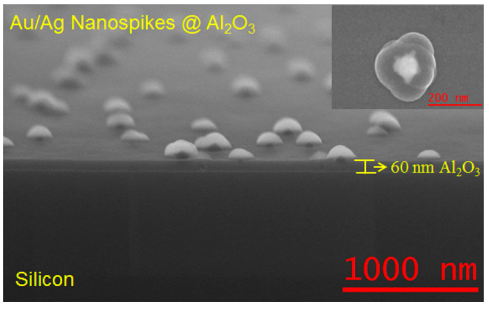

Figure 9. Cross-sectional SEM micrograph of the rear side of a solar cell with the embedded Au/Ag multispiked NPs on a 60 nm ALD Al_2O_3 film. The inset in the upper right corner depicts the top view of a single Au/Ag multispiked NP coated with the Al_2O_3 film.

The $J-V$ curves for the devices with Au and Ag NPs on the rear surface are also plotted on the same graph for comparison. The average photovoltaic performance parameters of the described devices are summarized in Table 1.

J_{SC} and V_{OC} values of 21.43 mA/cm^2 and 542 mV, respectively, have been measured for a cell having Au/Ag multispiked NPs on its rear surface, which leads to a promising power conversion efficiency (PCE) value of 7.70% for an ultrathin hybrid heterojunction cell fabricated in a 12 μm planar single crystal silicon membrane

Ostensibly, those values correspond well to the values of J_{SC} and V_{OC} of 19.64 mA/cm^2 and 530 mV, respectively, that were recorded for a similar cell without the plasmonic Au/Ag multispiked NPs. Intermediate values were collected when employing Au (PCE of 7.06%) and Ag nanoparticles (PCE of 7.30%). The PCE of the described device technology can be further increased by employing a front surface light trapping scheme. The experimental observations suggest that light

dx.doi.org/10.1021/am5040939 | ACS Appl. Mater. Interfaces 2014, 6, 15472−15479

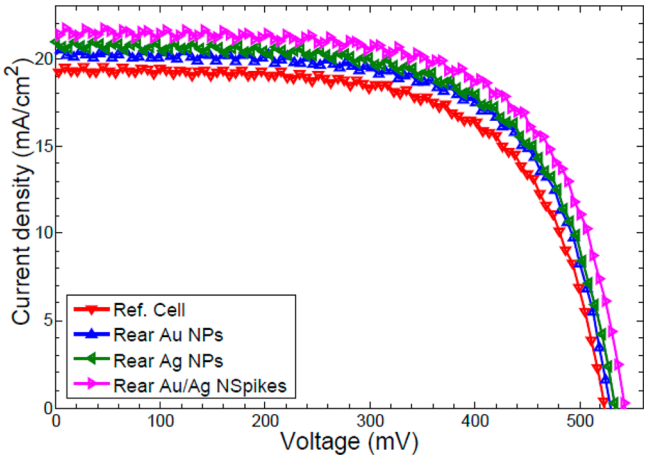

Figure 10. Measured current density versus voltage ($J-V$) curve for the fabricated Si/PEDOT:PSS hybrid devices with and without rear surface Au/Ag multispiked NPs. $J-V$ curves for the devices with Au and Ag NPs on the rear surface are also included for comparison.

Table 1. Measured Photovoltaic Performance Parameters, Including Open Circuit Voltage (V_{OC}), Short Circuit Current Density (J_{SC}), Fill Factor (*FF*), and Power Conversion Efficiency (*PCE*), for the Described Ultrathin Si/PEDOT:PSS Hybrid Solar Cells with and without Plasmonic NPs on the Rear Surface of the Devices

cell types	V_{OC} (mV)	J_{SC} (mA/cm^2)	FF (%)	PCE (%)
ref. cell	530	19.64	64.9	6.72
rear Au NPs	535	20.14	66.0	7.06
rear Ag NPs	537	20.62	65.8	7.30
Au/Ag multispiked	542	21.43	66.0	7.70

trapping by multispiked nanoparticles is a promising route for a sizable PCE increase, due to plasmon effects, in thin-film, c-Si solar cells in the near future.

4. CONCLUSIONS

Highly monodisperse, reasonably stable, multipode Au/Ag bimetallic nanostructures were synthesized by using an inorganic additive as a ligand for photovoltaic applications. The synthesized plasmonic nanoparticles were characterized by using high-resolution scanning electron microscopy and transmission electron microscopy along with the energy dispersive X-ray spectroscopy. Raman shift measurements along with UV−vis absorbance measurements for the Au/Ag multispiked nanoparticles corroborated a strong plasmon effect of those structures, which compared favorably well with Au and Ag nanospheres. The nanostructures were employed in the fabrication of ultrathin planar Si/PEDOT:PSS heterojunction solar cells with and without plasmonic nanoparticles on the rear surface. The homogeneous particle distribution on the surface was attained by the utilization of a porous anodized alumina template. A power conversion efficiency (PCE) value as high as 7.70% has been observed on devices having Au/Ag multispiked nanoparticles on the rear surface of c-silicon membranes (~12 μm), outperforming devices without nanoparticles or those solely with Au or Ag nanospheres.

■ ASSOCIATED CONTENT

Supporting Information

Video S1 showing a free-standing porous anodized alumina template floating in water. Figures S1 and S2 with HAADF-STEM images depicting the different shapes of spikes of the Au/Ag multispiked particles and the corresponding elemental maps. Figure S3 depicting the embedded Ag NPs inside the ALD deposited Al_2O_3 on the rear surface of the cell. This material is available free of charge via the Internet at http://pubs.acs.org.

■ AUTHOR INFORMATION

Corresponding Author

*Phone: 210-458-7245. E-mail: Arturo.Ayon@utsa.edu.

Notes

The authors declare no competing financial interest.

■ ACKNOWLEDGMENTS

We thank the U.S. Army Research Office for the financial support provided for this project (ARO Grant Number W911NF-13-1-0110).

■ REFERENCES

(1) Atwater, H. A.; Polman, A. Plasmonics for Improved Photovoltaic Devices. *Nat. Mater.* **2010**, *9*, 205−213.
(2) Pudasaini, P. R.; Ayon, A. A. Nanostructured Thin Film Silicon Solar Cells Efficiency Improvement Using Gold Nanoparticles. *Phys. Status Solidi A* **2012**, *209*, 1475−1480.
(3) Hägglund, C.; Apell, S. P. Plasmonic Near-Field Absorbers for Ultrathin Solar Cells. *J. Phys. Chem. Lett.* **2012**, *3*, 1275−1285.
(4) Lu, L.; Luo, Z.; Xu, T.; Yu, L. Cooperative Plasmonic Effect of Ag and Au Nanoparticles on Enhancing Performance of Polymer Solar Cells. *Nano Lett.* **2012**, *13*, 59−64.
(5) Lee, D. H.; Kwon, J. Y.; Maldonado, S.; Tuteja, A.; Boukai, A. Extreme Light Absorption by Multiple Plasmonic Layers on Upgraded Metallurgical Grade Silicon Solar Cells. *Nano Lett.* **2014**, *14*, 1961−1967.
(6) Stratakis, E.; Kymakis, E. Nanoparticle-Based Plasmonic Organic Photovoltaic Devices. *Mater. Today* **2013**, *16*, 133−146.
(7) Gan, Q.; Bartoli, F. J.; Kafafi, Z. H. Organic Photovoltaics: Plasmonic-Enhanced Organic Photovoltaics: Breaking the 10% Efficiency Barrier. *Adv. Mater.* **2013**, *25*, 2377.
(8) Tan, H.; Santbergen, R.; Smets, A. H. M.; Zeman, M. Plasmonic Light Trapping in Thin-film Silicon Solar Cells with Improved Self-Assembled Silver Nanoparticles. *Nano Lett.* **2012**, *12*, 4070−4076.
(9) Kalfagiannis, N.; Karagiannidis, P. G.; Pitsalidis, C.; Panagiotopoulos, N. T.; Gravalidis, C.; Kassavetis, S.; Patsalas, P.; Logothetidis, S. Plasmonic Silver Nanoparticles for Improved Organic Solar Cells. *Sol. Energy Mater. Sol. Cells* **2012**, *104*, 165−174.
(10) Nakayama, K.; Tanabe, K.; Atwater, H. A. Plasmonic Nanoparticle Enhanced Light Absorption in GaAs Solar Cells. *Appl. Phys. Lett.* **2008**, *93*, 121904(1)−121904(3).
(11) Kwon, J. Y.; Lee, D. H.; Chitambar, M.; Maldonado, S.; Tuteja, A.; Boukai, A. High Efficiency Thin Upgraded Metallurgical-Grade Silicon Solar Cells on Flexible Substrates. *Nano Lett.* **2012**, *12*, 5143−5147.
(12) Spinelli, P.; Verschuuren, M. A.; Polman, A. Broadband Omnidirectional Antireflection Coating Based on Subwavelength Surface Mie Resonators. *Nat. Commun.* **2012**, *3*, 692.
(13) Yang, Y.; Pillai, S.; Mehrvarz, H.; Kampwerth, H.; Ho-Baillie, A.; Green, M. A. Enhanced Light Trapping for High Efficiency Crystalline Folar Cells by the Application of Rear Surface Plasmons. *Sol. Energy Mater. Sol. Cells* **2012**, *101*, 217−226.
(14) Hägglund, C.; Zeltzer, G.; Ruiz, R.; Thomann, I.; Lee, H.-B.-R.; Brongersma, M. L.; Bent, S. F. Self-Assembly Based Plasmonic Arrays

Tuned by Atomic Layer Deposition for Extreme Visible Light Absorption. *Nano Lett.* **2013**, *13*, 3352−3357.
(15) Beck, F. J.; Mokkapati, S.; Catchpole, K. R. Plasmonic Light-Trapping for Si Solar Cells Using Self-assembled, Ag Nanoparticles. *Prog. Photovoltaics* **2010**, *18*, 500−504.
(16) Munday, J. N.; Atwater, H. A. Large Integrated Absorption Enhancement in Plasmonic Solar Cells by Combining Metallic Gratings and Antireflection Coatings. *Nano Lett.* **2010**, *11*, 2195−2201.
(17) Pillai, S.; Catchpole, K. R.; Trupke, T.; Green, M. A. Surface Plasmon Enhanced Silicon Solar Cells. *J. Appl. Phys.* **2007**, *101*, 093105(1)−093105(8).
(18) Wen, L.; Sun, F.; Chen, Q. Cascading Metallic Gratings for Broadband Absorption Enhancement in Ultrathin Plasmonic Solar Cells. *Appl. Phys. Lett.* **2014**, *104*, 151106(1)−151106(5).
(19) Pudasaini, P. R.; Ayon, A. A. Nanostructured Plasmonics Silicon Solar Cells. *Microelectron. Eng.* **2013**, *110*, 126−131.
(20) El Daif, O.; Tong, L.; Figeys, B.; Van Nieuwenhuysen, K.; Dmitriev, A.; Van Dorpe, P.; Gordon, I.; Dross, F. Front Side Plasmonic Effect on Thin Silicon Epitaxial Solar Cells. *Sol. Energy Mater. Sol. Cells* **2012**, *104*, 58−63.
(21) Fahim, N. F.; Ouyang, Z.; Jia, B.; Zhang, Y.; Shi, Z.; Gu, M. Enhanced Photocurrent in Crystalline Silicon Solar Cells by Hybrid Plasmonic Antireflection Coatings. *Appl. Phys. Lett.* **2012**, *101*, 261102(1)−261102(5).
(22) Diukman, I.; Orenstein, M. How Front Side Plasmonic Nanostructures Enhance Solar Cell Efficiency. *Sol. Energy Mater. Sol. Cells* **2011**, *95*, 2628−2631.
(23) Chen, X.; Jia, B.; Zhang, Y.; Gu, M. Exceeding the Limit of Plasmonic Light Trapping in Textured Screen-Printed Solar Cells Using Al Nanoparticles and Rinkle-like Graphene Sheets. *Light: Sci. Appl.* **2013**, *2*, e92.
(24) Sharma, M.; Pudasaini, P. R.; Ruiz-Zepeda, F.; Elam, D.; Ayon, A. A. Ultrathin, Flexible Organic−Inorganic Hybrid Solar Cells Based on Silicon Nanowires and PEDOT:PSS. *ACS Appl. Mater. Interfaces* **2014**, *6*, 4356−4363.
(25) Park, J.; Park, N.; Varlamov, S. Optimum Surface Condition for Plasmonic Ag Nanoparticles in Polycrystalline Silicon Thin Film Solar Cells. *Appl. Phys. Lett.* **2014**, *104*, 033903(1)−033903(4).
(26) Wang, P. H.; Millard, M.; Brolo, A. G. Optimizing Plasmonic Silicon Photovoltaics with Ag and Au Nanoparticle Mixtures. *J. Phys. Chem. C* **2014**, *118*, 5889−5895.
(27) Liang, H.; Wang, W.; Huang, Y.; Zhang, S.; Wei, H.; Xu, H. Controlled Synthesis of Uniform Silver Nanospheres. *J. Phys. Chem. C* **2010**, *114*, 7427−7431.
(28) Gao, C.; Vuong, J.; Zhang, Q.; Liu, Y.; Yin, Y. One-step Seeded Growth of Au Nanoparticles with Widely Tunable Sizes. *Nanoscale* **2012**, *4*, 2875−2878.
(29) Masuda, H.; Fukuda, K. Ordered Metal Nanohole Arrays Made by a Two-Step Replication of Honeycomb Structures of Anodic Alumina. *Science* **1995**, *268*, 1466−1468.
(30) Sangar, A.; Merlen, A.; Torchio, P.; Vedraine, S.; Flory, F.; Escoubas, L.; Patrone, L.; Delafosse, G.; Chevallier, V.; Moyen, E.; Hanbucken, M. Ordered Metal Nanohole Arrays Made by a Two-Step Replication of Honeycomb Structures of Anodic Alumina. *Sol. Energy Mater. Sol. Cells* **2013**, *117*, 657−662.
(31) Mayoral, A.; Magen, C.; Jose-Yacaman, M. High Yield Production of Long Branched Au Nanoparticles Characterized by Atomic Resolution Transmission Electron Microscopy. *Cryst. Growth Des.* **2011**, *11*, 4538−4543.
(32) Liu; Guyot-Sionnest, P. Mechanism of Silver(I)-Assisted Growth of Gold Nanorods and Bipyramids. *J. Phys. Chem. B* **2005**, *109*, 22192−22200.
(33) Zhang, X.; Tsuji, M.; Lim, S.; Miyamae, N.; Nishio, M.; Hikino, S.; Umezu, M. Synthesis and Growth Mechanism of Pentagonal Bipyramid-Shaped Gold-Rich Au/Ag Alloy Nanoparticles. *Langmuir* **2007**, *23*, 6372−6376.
(34) Yuen, C.; Zheng, W.; Huang, Z.; Yuen, C.; Zheng, W.; Huang, Z. Improving Surface-Enhanced Raman Scattering Effect Using Gold-Coated Hierarchical Polystyrene Bead Substrates Modified with Postgrowth Microwave Treatment. *J. Biomed. Opt.* **2008**, *13*, 064040(1)−064040(5).
(35) Hildebrandt, P.; Stockburger, M. Surface-Enhanced Resonance Raman Spectroscopy of Rhodamine 6G Adsorbed on Colloidal Silver. *J. Phys. Chem.* **1984**, *88*, 5935−5944.
(36) Stiles, P. L.; Dieringer, J. A.; Shah, N. C.; Van Duyne, R. P. Surface-Enhanced Raman Spectroscopy. *Annu. Rev. Anal. Chem.* **2008**, *1*, 601−626.
(37) Loo, B. H.; Furtak, T. E. The Giant Raman Effect From Pyridine on a Chemically Modified Gold Substrate. *Chem. Phys. Lett.* **1980**, *71*, 68−71.
(38) Hao, F.; Nehl, C. L.; Hafner, J. H.; Nordlander, P. Plasmon Resonances of a Gold Nanostar. *Nano Lett.* **2007**, *7*, 729−732.
(39) Nehl, C. L.; Liao, H.; Hafner, J. H. Optical Properties of Star-Shaped Gold Nanoparticles. *Nano Lett.* **2006**, *6*, 683−688.
(40) Fales, A. M.; Yuan, H.; Vo-Dinh, T. Development of Hybrid Silver-Coated Gold Nanostars for Nonaggregated Surface-Enhanced Raman Scattering. *J. Phys. Chem. C* **2014**, *118*, 3708−3715.
(41) Chen, J.; Martensson, T.; Dick, K. A.; Deppert, K.; Xu, H. Q.; Samuelson, L.; Xu, H. Surface-Enhanced Raman Scattering of Rhodamine 6G on Nanowire Arrays Decorated with Gold Nanoparticles. *Nanotechnology* **2008**, *19*, 275712(1)−275712(5).
(42) Pudasaini, P. R.; Ruiz-Zepeda, F.; Sharma, M.; Elam, D.; Ponce, A.; Ayon, A. A. High Efficiency Hybrid Silicon Nanopillar−Polymer Solar Cells. *ACS Appl. Mater. Interfaces* **2013**, *5*, 9620−9627.
(43) He, L.; Jiang, C.; Wang, H.; Lai, D.; Rusli. Si Nanowires Organic Semiconductor Hybrid Heterojunction Solar Cells Toward 10% Efficiency. *ACS Appl. Mater. Interfaces* **2012**, *4*, 1704−1708.
(44) Jeong, S.; Garnett, E. C.; Wang, S.; Yu, Z.; Fan, S.; Brongersma, M. L.; McGehee, M. D.; Cui, Y. Hybrid Silicon Nanocone−Polymer Solar Cells. *Nano Lett.* **2012**, *12*, 2971−2976.